



Originally published as:

Wang, H., Zhang, K. D., Wan, X., Lühr, H. (2017): Universal time variation of high-latitude thermospheric disturbance wind in response to a substorm. - *Journal of Geophysical Research*, 122, 4, pp. 4638—4653.

DOI: <http://doi.org/10.1002/2016JA023630>

RESEARCH ARTICLE

10.1002/2016JA023630

Universal time variation of high-latitude thermospheric disturbance wind in response to a substorm

Hui Wang¹ , Ke Deng Zhang¹, Xin Wan¹, and Hermann Lühr²¹Department of Space Physics, School of Electronic Information, Wuhan University, Hubei, China, ²GFZ German Research Center for Geosciences, Potsdam, Germany

Key Points:

- Physical mechanisms for substorm disturbance winds change with magnetic local time and vary for wind components
- Ion drag is the major driver for both meridional and zonal disturbance winds, and viscous force is effective in resistance to ion drag
- The disturbance winds exhibit larger variations with universal time at equinox and winter in comparison to summer

Supporting Information:

- Supporting Information S1

Correspondence to:

H. Wang,
h.wang@whu.edu.cn

Citation:

Wang, H., K. D. Zhang, X. Wan, and H. Lühr (2017), Universal time variation of high-latitude thermospheric disturbance wind in response to a substorm, *J. Geophys. Res. Space Physics*, 122, 4638–4653, doi:10.1002/2016JA023630.

Received 25 OCT 2016

Accepted 24 MAR 2017

Accepted article online 29 MAR 2017

Published online 21 APR 2017

Abstract The temporal and spatial variation in thermospheric winds are studied at 400 km altitude in response to substorms that start at different universal time (UT), using a global ionosphere and thermosphere model. The substorm-induced disturbance winds at high latitudes are mainly in the poleward, westward, and upward directions in the dusk sector and in the equatorward, westward, and upward directions in the nighttime. The daytime perturbation is due to ion drag, driven by variations in interplanetary magnetic field B_z , whereas the nighttime perturbation is due to both the B_z and hemispheric power input. The nightside disturbed winds respond somewhat later than the dayside owing to low background ion density. Ion drag is the dominant driving force in the daytime for both meridional and zonal disturbed winds, whereas Joule heating is the dominant factor for the vertical winds. The nighttime meridional and zonal winds are driven by a combination of ion drag, Joule heating, and heating of the auroral belt, whereas the vertical winds are mainly caused by auroral belt heating. The viscous force acts to resist the ion drag, whereas the Coriolis force is negligible. The disturbed winds exhibit large variations with UT during equinox and local winter conditions. With more solar illumination, stronger disturbed winds can be generated. Weak or even opposite variations with UT in the disturbed winds are found in local summer, which is due to a smaller UT variation of the daytime ion density and a larger contribution from auroral heating than from ion drag.

Plain Language Summary Thermospheric winds play vital roles in the ion-neutral interactions, which are key processes in the modeling and forecasting of space weather. The physical mechanics of universal time dependence of substorms effect on neutral wind and the extent of its effects have not been addressed in the literature. The present work found some interesting results as following: (1) Physical mechanisms for substorm disturbance winds change with magnetic local time and vary for wind components. (2) Ion drag forces are predominant driving forces for both meridional and zonal disturbance winds, and viscous force is effective in resistance to ion drag. (3) The disturbance winds exhibit larger variations with universal time at equinox and winter in comparison to summer.

1. Introduction

Thermospheric winds play a vital role in ion-neutral interactions, which are key processes in space weather. They can transport plasma along magnetic field lines [e.g., *Rishbeth*, 1967], generate electric fields via the dynamo effect [e.g., *Blanc and Richmond*, 1980], and drive plasma convection and Hall and field-aligned current systems via the flywheel effect [e.g., *Deng et al.*, 1993]. Therefore, they have been studied extensively during the past few decades by both observations and modeling [*Richmond and Matsushita*, 1975; *McCormac and Smith*, 1984; *Thayer et al.*, 1987; *Emmert et al.*, 2002; *Richmond et al.*, 2003; *Deng and Ridley*, 2006; *Emmert et al.*, 2006a, 2006b; *Lühr et al.*, 2007; *Ritter et al.*, 2010; *Wang et al.*, 2012; *Xiong et al.*, 2015a, 2015b; *Wang and Luehr*, 2016],

The global neutral wind in the F region is driven by a combination of pressure gradients induced by local or global heating, ion drag, Coriolis and centrifugal forces, and upward propagating atmospheric tides [e.g., *Richmond et al.*, 2003]. During quiet times the ion drag force is considered to be of primary importance at high latitudes [e.g., *Thayer et al.*, 1987; *Thayer and Killeen*, 1993; *Richmond et al.*, 2003; *Lühr et al.*, 2007], where the neutral wind pattern is strongly influenced by ion convection, which consists of fast antisunward flow over the polar cap and sunward ion flows at auroral latitudes on both the dawn and dusk sides. The neutral

clockwise cell on the duskside is stronger than the anticlockwise cell on the dawnside, which is attributed to the combined action of ion drag and Coriolis force [e.g., *Killeen and Roble*, 1984; *Lühr et al.*, 2007]. Previous work has investigated the solar cycle and seasonal variations in high-latitude winds and their response to interplanetary magnetic field (IMF), which are, in general, in agreement with an ion drag mechanism [e.g., *McCormac and Smith*, 1984; *Emmert et al.*, 2006a, 2006b; *Lühr et al.*, 2007].

During geomagnetically disturbed periods, the thermospheric winds are highly disturbed in response to both an increased input of auroral energy (both Joule and particle precipitation heating) and enhanced plasma convection. Previous work mainly focused on the effect of magnetic activity on the thermospheric winds. *Babcock and Evans* [1979] reported stronger equatorward disturbed winds on the nightside based on observations from the Millstone Hill radar. By using wind measurements from the Wind Imaging Interferometer on the UARS satellite, *Emmert et al.* [2001] found that midlatitude disturbance winds are mostly westward with the greatest speeds appearing in the late afternoon. Based on observations of zonal winds by the CHAMP satellite, *Xiong et al.* [2015b] revealed that the disturbed winds ($Kp > 2$) display quite different diurnal variations in the auroral and subauroral latitude bands ($50^\circ - 70^\circ$ magnetic latitude, MLAT) in comparison to quiet periods. They found that there is no modification of wind in the local time sector from midnight to 0900 magnetic local time (MLT). From 1500 to 2000 MLT they found a strong westward disturbed wind. Based on zonal wind observations from CHAMP, *Ritter et al.* [2010] compared the substorm-related disturbed winds during successive orbits in the nighttime from 2100 to 0300 MLT. They reported that the increase in the westward disturbed wind is about 50 m/s at midlatitudes around midnight.

Previous work has debated the relative importance of Joule heating and sources of ion drag in disturbing neutral winds [e.g., *Richmond and Matsushita*, 1975; *Roble et al.*, 1982; *Robinson et al.*, 1987; *Fuller-Rowell et al.*, 1994]. However, quite contrary results are received by using different models (2-D or 3-D) with different drivers (long term or short term). One of the objectives of this paper is to extract the different mechanisms of disturbed winds during substorm periods. The different mechanisms in the daytime and nighttime are also explored. This kind of work has not been undertaken in the literature. A 3-D self-consistent global ionosphere thermosphere model (GITM) [e.g., *Ridley et al.*, 2006] is utilized. The magnetospheric energy inputs are based on a superposed epoch analysis of solar and geomagnetic conditions [*Clausen et al.*, 2014] by using the extensive substorms onset events from 2001 to 2005 [*Frey and Mende*, 2006].

The displacement of the geographic and geomagnetic poles can introduce a universal time (UT) effect on both ion drag and Joule heating forces, which may cause a UT-dependent response in the thermosphere. Another aim of the present work is to extract and explain the UT effect of substorm processes on the neutral wind in different local times. Previous studies of UT effects focused on either the effect of magnetic storms or effects on parameters such as neutral mass density and temperature. For example, *Roble et al.* [1982] examined the effect of the cross polar cap potential of 120 kV with extended period of 3 days on neutral winds and temperature. They found that both meridional and zonal disturbed winds peak around 1800 (0600) UT in the Northern (Southern) Hemisphere during storm periods. *Fuller-Rowell et al.* [1994] used a coupled ionosphere-thermosphere model to illustrate the response of the ionosphere and thermosphere to geomagnetic storms. A storm was characterized by an increase in magnetospheric energy input at high latitudes for a 12 h period. Four storms commence at different UTs at an interval of 6 h. They found that the Joule heating drove a traveling atmospheric disturbance (TAD) from polar to low latitudes and into the opposite hemisphere. The maximum propagation speed of TADs occurred in the sector closest to the magnetic pole and on the nightside. The minimum response occurred in the sector farthest from the magnetic pole and when this sector was on the dayside. *Fujiwara et al.* [1996] conducted two numerical simulations, one having an energy injection of 1 h representative of a substorm type and the other having a 12 h energy injection representative of a storm type. They suggested that the substorm energy injection preferentially generated atmospheric gravity wave which transferred energy through adiabatic heating and cooling, while the storm energy injection was more effective in generating a meridional circulation which transferred energy by both advective and adiabatic processes. By using GITM simulations, *Perlongo and Ridley* [2016] investigated the polar-averaged thermospheric air mass density and temperature in response to increased polar convection velocities based on the UT. They found that the highest air mass density and temperature are at those times when the geomagnetic pole is pointing toward the Sun. This orientation makes the region of maximum solar ionization collocated with the high-latitude potential pattern, leading to more Joule heating. Thus, although

the wind response to full geomagnetic storms and the density response to substorms have been studied, the extent and mechanics of a UT effect by substorms on neutral winds have not been addressed and quantified in the literature.

The equinoxes are favorable for geomagnetic activity, which has variously been explained by the interaction efficiency of the solar wind [e.g., *Russell and McPherron, 1973; Temerin and Li, 2002*] or by solar illumination conditions [e.g., *Lyatsky et al., 2001*]. Previous work [*Wang and Lühr, 2007*] disclosed that 1200 UT on the December solstice and 2400 UT on the June solstice are more favorable for substorms to occur. The ionospheric Pedersen conductances from both hemispheres induced by solar illumination in the nightside auroral regions can explain the seasonal and UT dependences of the frequency of substorm occurrence. In contrast to these studies on solar wind-magnetosphere-ionosphere coupling, the present work investigates the ionosphere-thermosphere coupling based on the GITM; that is, it primarily examines the response of the thermospheric disturbed wind to the same level of forcing by magnetospheric substorms, but starting at different UTs.

2. Model

The global ionosphere thermosphere model (GITM) is a three-dimensional model that simulates the ionosphere and thermosphere dynamics and was developed at the University of Michigan. A complete description of the model can be found in *Ridley et al. [2006]*. The model solves the continuity, momentum, and energy equations in the thermosphere and ionosphere using realistic source terms. The neutral momentum equation is solved by considering the pressure gradients, ion drag, viscous force, and Coriolis force. GITM is driven by the high-latitude electric field [*Weimer, 2005*], precipitation of auroral particles [*Fuller-Rowell and Evans, 1987*], solar extreme ultraviolet (EUV) radiation, and tides (global-scale wave model) at the lower boundary [*Hagan et al., 1999*]. GITM is initiated by using mass spectrometer-incoherent scatter [*Hedin, 1991*] and International Reference Ionosphere [*Bilitza, 2001*] neutral and ion densities and temperatures. The magnetic topology can be described by either the dipole field or the International Geomagnetic Reference Field (IGRF epoch 2010) [*Maus et al., 2005*]. Except as noted below, the IGRF model is adopted in the simulation. Following *Richmond et al. [2003]*, the results are ordered in the frame of quasi-dipole (QD) coordinates as defined in *Richmond [1995]*. The base vector \mathbf{f}_2 , defined in *Richmond [1995]*, points along the QD meridians. To be consistent with the coordinate system and to be more physically meaningful, the model output wind components in geographic coordinate system are converted into the QD coordinate system, where U_n and U_e are meridional and zonal winds in QD coordinates, U_{gn} and U_{ge} are meridional and zonal winds in geographic coordinates, D is the angle between \mathbf{f}_2 and geographic north: $U_n = U_{gn} \times \cos D + U_{ge} \times \sin D$, $U_e = -U_{gn} \times \sin D + U_{ge} \times \cos D$. Fortran code for determining QD coordinates and the associated basis vector is available in the supporting information of *Emmert et al. [2010]*.

For this study, GITM was run with a resolution of 5° latitude by 10° longitude and with a stretched altitude, resolving the vertical scales with approximately one third of a scale height. It was run for 48 h to reach a quasi steady state. Simulations were then continued from the startup simulation for another 24 h from 21 March 00:00 UT. The input parameters for a quiet time run were as follows: IMF $B_x = -2$ nT, $B_y = 2$ nT, $B_z = 0$ nT, solar wind velocity, $V_x = 400$ km/s, $F_{10.7} = 100$ solar flux unit, and hemispheric power (HP) = 20 GW. The tides at the lower boundary were turned off in order to check the in situ physical processes.

A substorm-related input was constructed based on a superposed epoch analysis applied to IMF B_z and hemispheric power (HP) during 5 years of substorm events [*Clausen et al., 2014*]. Recent works [*Liu and Ridley, 2015; Zhu et al., 2016*] have utilized GITM with the same inputs to study the effects of substorms on the thermospheric mass density and ionospheric temperature, and the start of the simulation presented in their work was also at 00:00 UT on 21 March. The modeled spatial and temporal variations of air mass density during substorm periods are in general consistent with those derived from CHAMP observations [*Clausen et al., 2014*]. Several studies have used GITM for ionosphere-thermosphere physical studies, and good agreements were achieved when model outputs were validated with observations and other modeling results [e.g., *Pawłowski and Ridley, 2009; Deng et al., 2011; Yiğit and Ridley, 2011; Ercha et al., 2012; Zhu and Ridley, 2014; Wang et al., 2015; Liu and Ridley, 2015; Wang and Luehr, 2016; Perlougo and Ridley, 2016*].

The temporal variations in IMF B_z and auroral activity (i.e., HP) used in the simulation are shown in Figure 1. The other solar wind and IMF parameters are the same as those during the quiet time. The 00:00 epoch time represents the onset of the substorm. IMF B_z begins to decrease at -60 min ($-1:00$ epoch time), reaches a

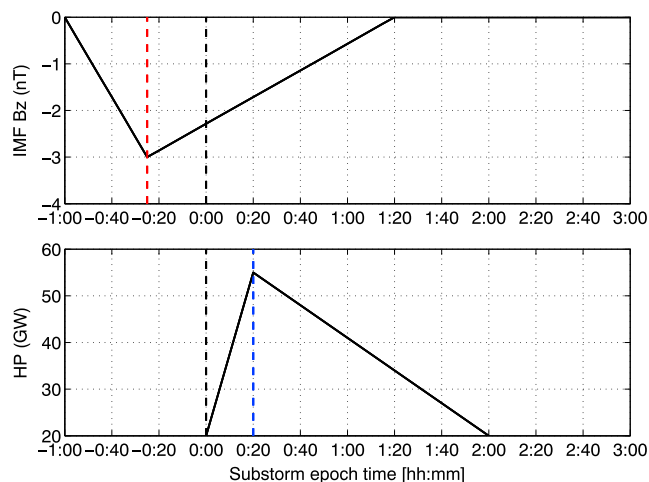


Figure 1. Temporal variations of IMF B_z and hemispheric power (HP) during an idealized substorm. The onset occurred at 0:00 epoch time, as indicated by the black vertical dashed line. The red (blue) vertical line indicates the time when IMF B_z (HP) reaches a minimum (maximum) value.

minimum of -3 nT at -25 min ($-0:25$), and recovers to the initial value of zero at 80 min (1:20). This represents the growth phase of the substorm, when energy is input into the magnetosphere via the dayside reconnection. This is consistent with previous findings that a northward turning of IMF B_z can sometimes trigger a substorm onset [e.g., Lyons, 1996; Wang and Lühr, 2007]. The background HP is 20 GW. It steadily increases after substorm onset, peaks at 55 GW at 20 min (representing the expansion phase), and recovers to 20 GW at 2:00 (recovery phase). This indicates that the substorm deposits an extra 55 GW in the polar regions. The substorm onset was artificially set to commence at different UTs, i.e., with start time separated by 2 h from 00:00 UT to 22:00 UT on 21 March. The situations at June and December solstices were also investigated. The perturbations associated with the substorm can be determined by considering the differences between substorm and quiet time runs.

3. Results

The model results in the following are presented at typical LEO (low Earth orbit) satellite heights of 400 km to make it compatible with observations published before. Figure 2 shows the variation with MLAT (50° – 90°) and MLT in the disturbed wind at 400 km. For the plotting an equal-area gridding is used. The inner ring from 90° to 85° is divided into 6 sectors, the second ring from 85° to 80° into 18 sectors, and so forth until 55° MLAT. The horizontal disturbance wind vector patterns including both meridional and zonal components are shown as black arrows, and the vertical disturbance wind is shown as colored contours. Positive values represent upward deflection. The variation is defined by $\Delta U = U_{ss} - U_{quiet}$, where U_{ss} is the wind during substorm periods. The quiet time winds U_{quiet} are the pattern at the same UT but 24 h earlier. ΔU values during the substorm at 20 min intervals from 60 min before the substorm onset to 160 min after the substorm onset are presented.

A strong variation in the horizontal wind vector pattern can be observed at polar latitudes. The disturbed wind starts first on the dayside, in direct response to the southward turning of IMF starting at $-1:00$. The clockwise cell in the dusk sector covers a wider area than the counterclockwise cell in the dawn sector. This pattern is similar to the ion convection pattern at that time (not shown). In the daytime the dusk cell is stronger than the dawn cell. These dawn-dusk asymmetries resemble the effect of positive IMF B_y on the ion convection [McCormac and Smith, 1984; Lühr et al., 2007]. The daytime disturbance wind attains a peak speed of about 196 m/s at $-0:10$ and then quickly disappears after 1:00 when IMF B_z returns to zero. At substorm onset (0:00), the disturbed winds appear on the nightside, first at dusk, and then at dawn (see 0:40). There are sunward flows at both dawn and dusk. The flow at dusk attains a peak around 0:30 at a speed of -82 m/s. The flow at dawn decreases in intensity after 1:30, whereas the dusk flow lasts for a longer time. One can find that the center of the nighttime equatorward wind shifts equatorward in the premidnight and early morning sectors. For example, at 0:10 the peak in the equatorward disturbed wind is located at 70° MLAT on the nightside, whereas at 1:00 it moves to 55° MLAT. This corresponds to a wave speed of about 590 m/s. The propagation speed is consistent with previous model and observational work reporting a phase speed of the equatorward

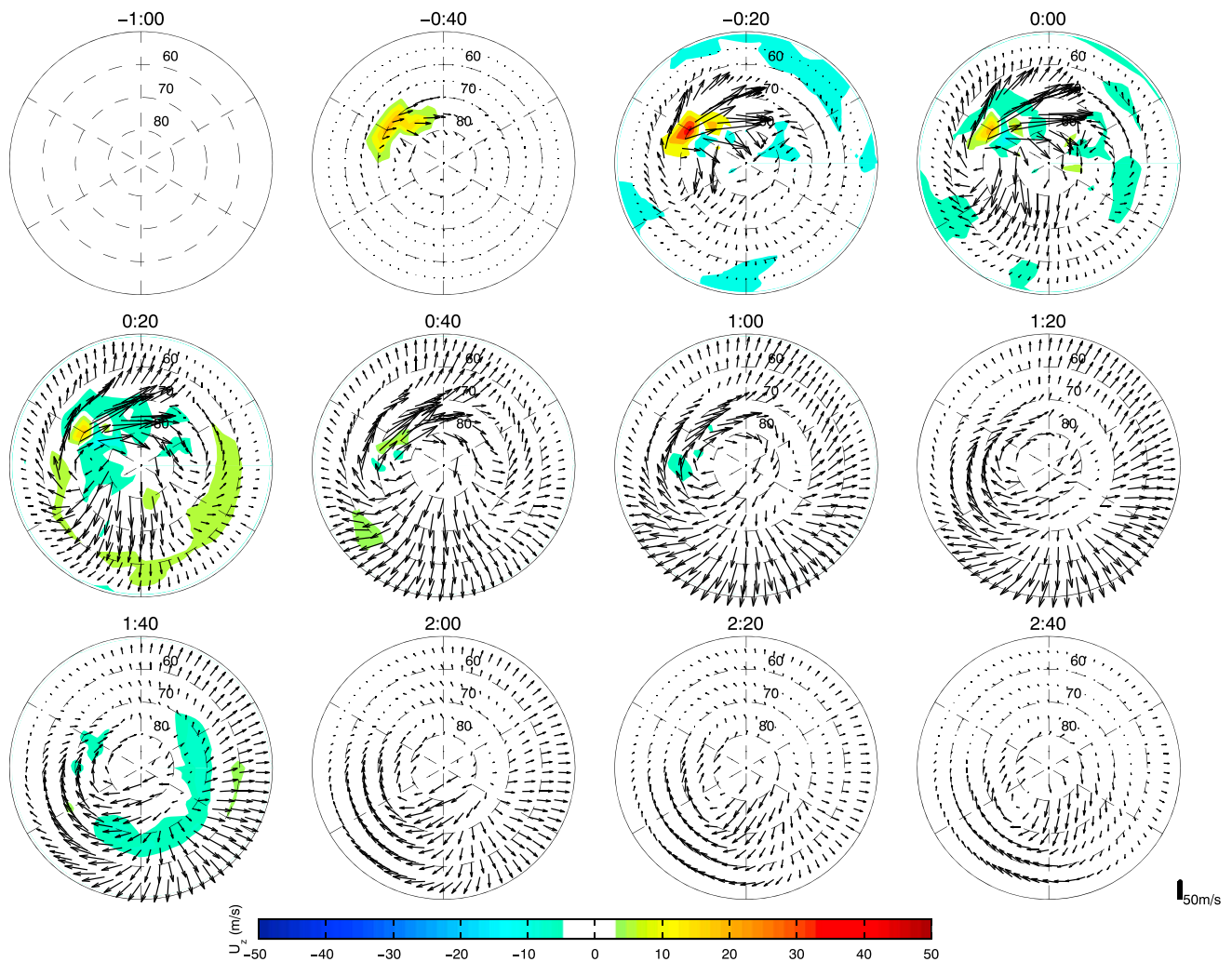


Figure 2. Geomagnetic latitude and magnetic local time variation of the thermospheric disturbed wind (ΔU) in the Northern Hemisphere, which is the difference between the substorm occurring at 00 UT and quiet time at 400 km altitude. Wind vectors in the horizontal planes are shown in black arrows, and the vertical wind is shown as colored contours. Positive values represent upward directions. The outer ring represents 50° MLAT. The substorm epoch time runs at 20 min intervals from -1 h to 2 h and 40 min. Noon is at the top of each panel. Midnight is at the bottom. Dawn is to the right and dusk to the left.

wind surge of about 600 m/s [e.g., Fuller-Rowell et al., 1994; Fujiwara et al., 1996; Ritter et al., 2010; Xiong et al., 2015b]. The peak vertical disturbed wind is about 40–50 m/s around $-0:20$, which is weaker in comparison to those in the horizontal directions. Upward deflection occurs mainly in the afternoon sector, with temporal variations related to IMF B_z . Upward winds in the nightside auroral oval appear after 0:10 in response to the hemispheric energy input with a peak amplitude of 10 m/s at 0:30.

Maps of zonal neutral winds during a substorm are derived from CHAMP observations by synchronizing data according to the substorm onset time within an interval of 15 min. The data were further bin averaged as a function of MLT and MLAT. No other smoothing algorithm is used. In case of a data gap, it is interpolated by using a triangulation-based nearest neighbor interpolation method. The polar map at $-1:00$ epoch time (1 h before substorm onset) is subtracted from maps at subsequent epoch times, in order to display the disturbed wind. The changes in cross-track wind observed by CHAMP are illustrated in Figure 3. Positive values represent eastward winds. The figure is constructed based on substorm events occurring around 00 UT (22–02 UT) at equinox (from March to May and from September to November) during the years from 2001 to 2005 [Frey and Mende, 2006]. Three epoch times at $-0:30$, 0:30, and 1:00 are shown for comparison with the model outputs, representing different phases of the substorm. The observed ΔU exhibit a two-cell convection pattern: clockwise cell at dusk and counterclockwise cell at dawn, which is similar in shape to the GITM results. Both the model and the observations reveal that the daytime westward ΔU attain peaks in the afternoon sector

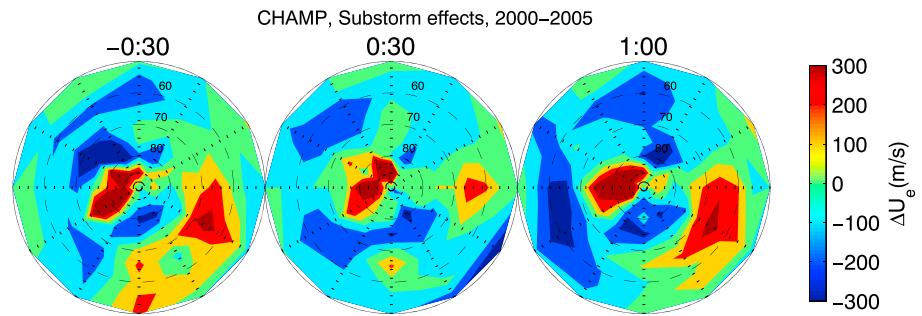


Figure 3. Same format as Figure 2 but for CHAMP cross-track wind observations at three epoch times.

during the substorm growth phase, and the nighttime sunward ΔU attain peaks during the recovery phase. The ΔU_e amplitudes from the model are underestimated, especially at dawn when compared to observations. The cross-track winds observed by CHAMP are predominantly in geographic zonal direction due to its high-inclination orbit, not in magnetic zonal direction. This could somewhat affect the comparison with GITM results. Our idealized numerical study is for one single day, driven by an average of solar wind and IMF condition during 5 year substorm periods (minimum IMF B_z of -2 nT for weak disturbed time, positive B_y of 2 nT). The CHAMP results were built up based on 5 year substorm results, which exhibit various ranges of IMF B_z and B_y in amplitude and polarity. Furthermore, model resolution can affect the magnitudes of outputs. *Deng and Ridley [2007]* found that when the latitudinal resolution increases from 5° to 1.5° , the neutral gas heating rate can increase by 20%, because the model can better capture small-scale electric field and particle precipitation. The purpose of the present work is not to validate the model. Instead, we try to use the comprehensive model to understand the underlying physics and mechanisms beneath the complexities on a fundamental level.

4. Discussion

4.1. Effect of Auroral Heating

The effects of auroral heating on the spatial and temporal evolution of neutral winds during disturbed periods were investigated by turning off the auroral heating term in the model. The differences between the auroral heating on and off runs are shown in Figure 4, which illustrates the auroral heating effect. Three epoch times ($-0:20$, $0:20$, and $1:00$) are presented, reflecting different phases of a substorm. It can be seen from Figure 4 that the disturbed winds are nearly zero during the growth phase at $-0:20$. This indicates the dominant role of other processes in affecting the dayside wind pattern during the growth phase. At $0:20$ and $1:00$ one can see that on the nightside both poleward and equatorward winds stem from the auroral belt, which is an expected signature of the heating by the auroral particle precipitation. The disturbed wind is stronger at $1:00$ in comparison to that at $0:20$. By comparison with Figure 2, one finds that heating of the auroral belt plays a vital role in causing sunward ΔU on both the dawn and dusk sides. The upward wind in the nighttime auroral oval arises from the heating by auroral precipitation particles (at $0:20$). The upward disturbed wind during the early phase of the substorm arises mainly from other processes as discussed below.

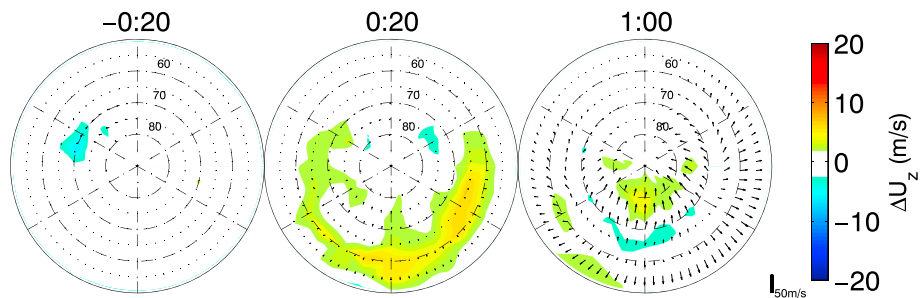


Figure 4. Geomagnetic latitude and magnetic local time variations of disturbed winds due to auroral heating for 00 UT substorm event. From left to right are results at $-0:20$, $0:20$, and $1:00$ epoch time. Wind vectors in the horizontal planes are shown, and vertical wind is shown as colored contour.

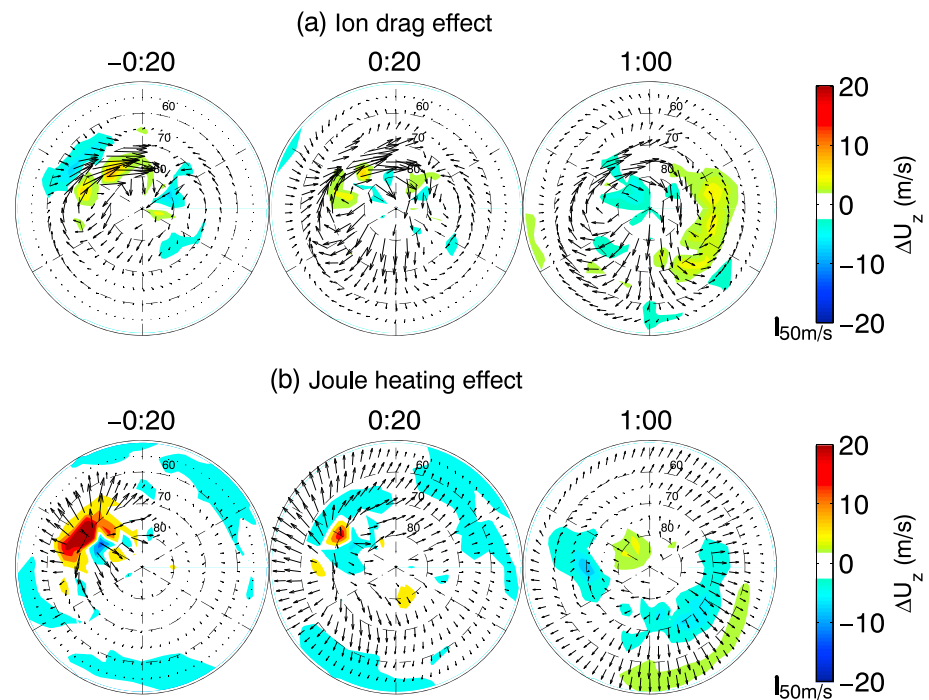


Figure 5. Same format as Figure 4 but for the (a) ion drag force and (b) Joule heating effect.

4.2. Relative Roles of Effects by Ion Drag and Joule Heating

Ion drag and Joule heating effects on winds were examined by turning off either the ion drag or Joule heating terms in the model. The differences between runs with and without one of the two terms can represent separately the effects. Figure 5 shows these separate effects from ion drag (a) and Joule heating (b) in the same format as Figure 4. It is obvious that in the daytime ion drag and Joule heating are dominant factors in disturbing the neutral wind, in comparison to heating of the auroral belt. The effect of ion drag is larger than that of Joule heating. For example, at $-0:20$, the poleward wind in the daytime due to ion drag is stronger by a factor of 2 than that caused by Joule heating, while the zonal wind caused by ion drag is stronger by a factor of 1.4 than that caused by Joule heating. Both ion drag and Joule heating contribute to the nighttime equatorward disturbance wind. The effect of ion drag on the equatorward wind is larger by a factor of 1.5 than that of Joule heating at $0:20$. The peak in Joule heating occurs around 110–150 km, at the altitude of maximum Pedersen conductivity [Deng and Ridley, 2007]. Thus, the effects of Joule heating at higher altitudes (400 km) can be relatively weak. By comparison with Figure 4, one finds that the auroral heating drives a poleward wind on the poleward side of the auroral oval, which is opposite to that produced by ion drag and/or Joule heating. With respect to the equatorward wind located at lower latitudes, both heating of the auroral belt heating and ion drag/Joule heating make constructive contributions. In the substorm recovery phase (1:00) the sunward flows in both the premidnight and postmidnight sectors are mainly caused by ion drag. The situation is different for the vertical disturbed wind (ΔU_z), where Joule heating is a key factor in driving upward winds in the afternoon during the substorm growth phase, whereas ion drag plays a relatively smaller role.

The product between the electron density and zonal wind, $\Delta n_e \times U_e$ (an important factor of ion drag force), from GITM is compared to that from CHAMP and shown in Figure 6 at three substorm epoch times. In both GITM and CHAMP results the daytime values attain peaks in the afternoon sector during the substorm growth phase. The nighttime values are weaker than those at dayside due to the low electron density at night. The values from GITM are again significantly lower than the CHAMP observations, but the patterns are similar.

4.3. Effects of Coriolis and Viscous Forces

To examine the Coriolis (or viscous force) effect on winds, we performed a simulation by turning off the term in the momentum function in the model. The differences between runs with and without the term can represent the Coriolis (or viscous) force effect. Figure 7 illustrates the effects of Coriolis and viscous forces on disturbed wind. The effect from viscous force is much larger than the effects from Coriolis, and almost in opposite phase

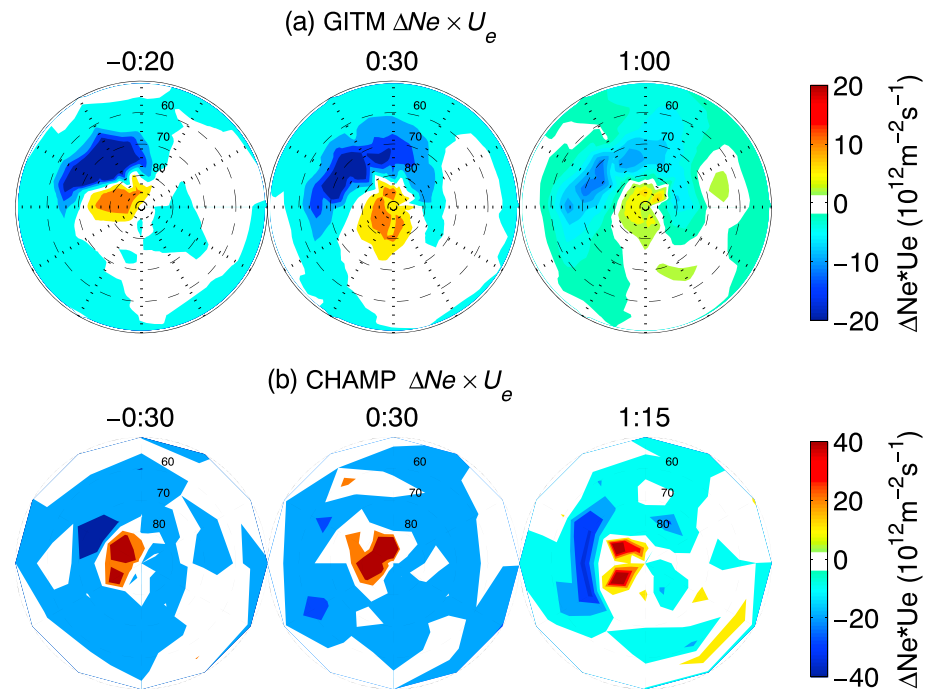


Figure 6. Geomagnetic latitude and magnetic local time variation in (a) GITM $\Delta N_e \times U_e$ and (b) CHAMP $\Delta N_e \times U_e$ for 00 UT substorm events. Three substorm epoch times are shown.

to the effect from ion drag, as shown in Figure 5. This is because ion drag is the predominant driving force for the substorm disturbed wind, and the viscous force is a responsive force to the wind. Reducing the altitude dependence, the viscous forces in the zonal and meridional direction are, $\frac{\partial}{\partial r} (\eta (\frac{\partial U_{gn}}{\partial r} + \frac{\partial U_{ge}}{\partial r}))$, where η is the coefficient of viscosity and r is in radial direction. The viscous force results do not really match any of the other forces, so the pattern is quite confusing. However, one can notice that at 0:20, the viscous force forms a strong antisunward flow in the dusk cell, which is opposite to the sunward flow driven by the ion drag. At 1:00, the wind pattern flows from the daytime to the nighttime due to viscous force. This is in opposite direction to the sunward flow around dawn and dusk sectors driven by the ion drag, indicating a drag force to the disturbed wind pattern driven by ion drag. One exception occurs around midnight where the wind pattern due to viscous force is in the same direction to the wind pattern driven by the ion drag.

In summary, the driving mechanisms of the disturbed winds during substorms display obvious variations with local time, and the wind components vary differently. In the daytime the horizontal disturbed winds are mainly driven by ion drag, whereas the vertical disturbed wind is driven by Joule heating. The nighttime disturbed winds respond somewhat later than the daytime winds. In the nighttime the meridional disturbed winds are driven by ion drag, Joule heating, and heating of the auroral belt. The zonal disturbed winds are mainly driven by ion drag and heating in the auroral belt. The vertical disturbed winds are mainly caused by heating in the auroral belt. The viscous forces act to resist the above driving forces and tend to reduce the disturbance wind pattern, whereas the Coriolis forces are relatively weak in modulating the disturbed winds.

4.4. Dependence on UT of Substorm Effects

This section focuses on variations with UT in substorm effects on neutral wind patterns. Substorms were started at intervals of 2 h from 00:00 UT to 22:00 UT. We focused on the peak deflections of winds in the poleward, westward, and upward directions in the daytime (0600–1800 MLT), as well as winds in the equatorward, westward, and upward directions in the nighttime (1800–0600 MLT). These are the strongest disturbance winds appearing in the high-latitude regions. The maps are included in electronic supplements, showing where the peak locations are at different UTs for selected substorm times.

The evolution with UT of these peak winds from –1:00 to 3:00 epoch time is shown in Figure 8. The variation with UT in disturbed winds is not induced by the cross-polar cap potential, as the variation with UT in the electric field in the model is slightly less than 2% [Weimer, 1996]. Generally speaking, cases occurring between

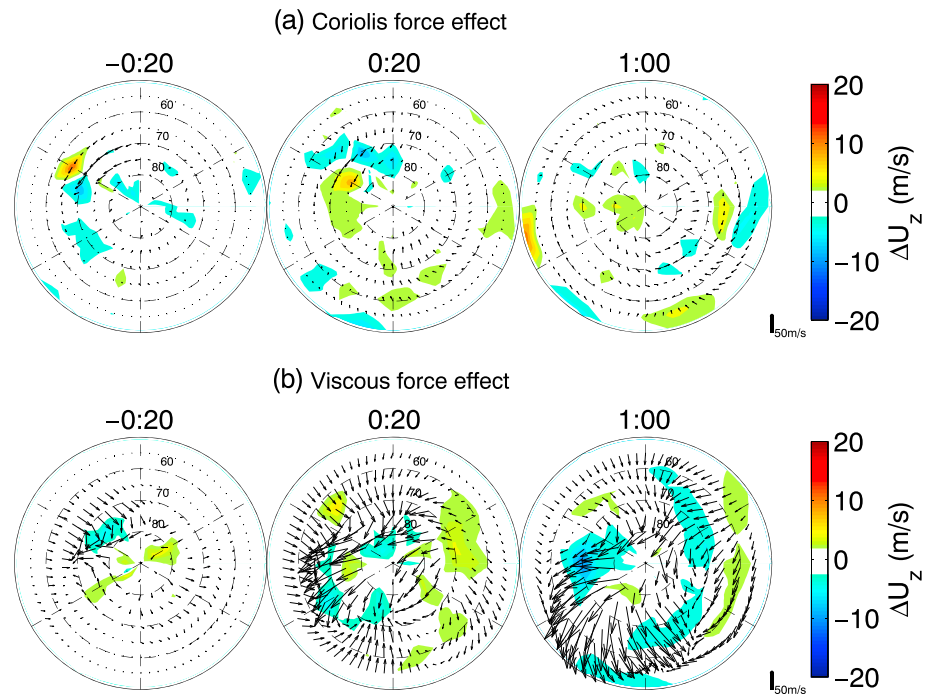


Figure 7. Same format as Figure 4 but for the (a) Coriolis force and (b) viscous force effect.

14:00 and 24:00 UT (reddish curves) take place in more sunlight than cases occurring at other UTs (bluish curves) in the north and vice versa in the south, and the peak disturbed winds are stronger in sunlight (reddish in the north and bluish in the south) than in darkness (bluish in the north and reddish in the south). Our GITM results are consistent with the model result of *Roble et al.* [1982], namely, that stronger winds are generated at 18:00 UT than at 06:00 UT in the Northern Hemisphere and vice versa in the Southern Hemisphere, although their results are for storm conditions.

The neutral winds respond rapidly to the southward turning of IMF B_z . For most substorm events the temporal variations in peak daytime winds are generally similar to those of IMF B_z , except for a time delay of about 10–20 min: IMF B_z attains a peak at $-0:25$, as indicated by the vertical red line; the meridional winds attain peaks at around $-0:10$; the zonal winds attain peaks at around $-0:05$; and the vertical winds attain peaks around $-0:20$. This is unsurprising because the daytime disturbed winds are driven mainly by increased ion drag, which is related to the increased velocity of ion convection in response to the southward turning of IMF B_z . The response in the nighttime occurs somewhat later for the meridional wind in comparison to the daytime, i.e., at 0:30 in the Northern Hemisphere and 0:00 in the Southern Hemisphere. The heating by auroral particles begins to take effect after 0:00.

In the Northern Hemisphere the nighttime westward zonal winds attain peaks around 0:20 to 1:20, i.e., 30–60 min later than on the dayside. In the Southern Hemisphere for some cases in sunlight (bluish curves), the zonal winds attain peaks at 0:00, i.e., at the same time as at daytime. This is believed to be in direct response to IMF B_z . When the nighttime polar cap is in sunlight, N_e on the nightside is high enough for ion drag to act rapidly and efficiently, in the same way as on the dayside. In contrast, when the polar cap on the nightside is in darkness, N_e is too low to allow winds to respond as rapidly as in the daytime. In Figures 8e and 8f the major peak in vertical wind on the nightside is related to Joule heating and exhibits a maximum around the time when B_z reaches a minimum. The secondary peak in the vertical wind is related to heating by the auroral belt precipitation and exhibits a maximum around the time when HP reaches a maximum.

Substantial UT dependencies appear in response of the disturbed winds. The maximum differences among peak disturbances are 118 m/s (129) for the poleward wind, 92 m/s (107) for the westward wind, and 43 m/s (48) for the upward wind in the daytime in the Northern (Southern) Hemisphere. In the nighttime the largest differences are 59 m/s (89) for the equatorward wind, 23 m/s (78) for the westward wind, and 10 m/s (19) for the

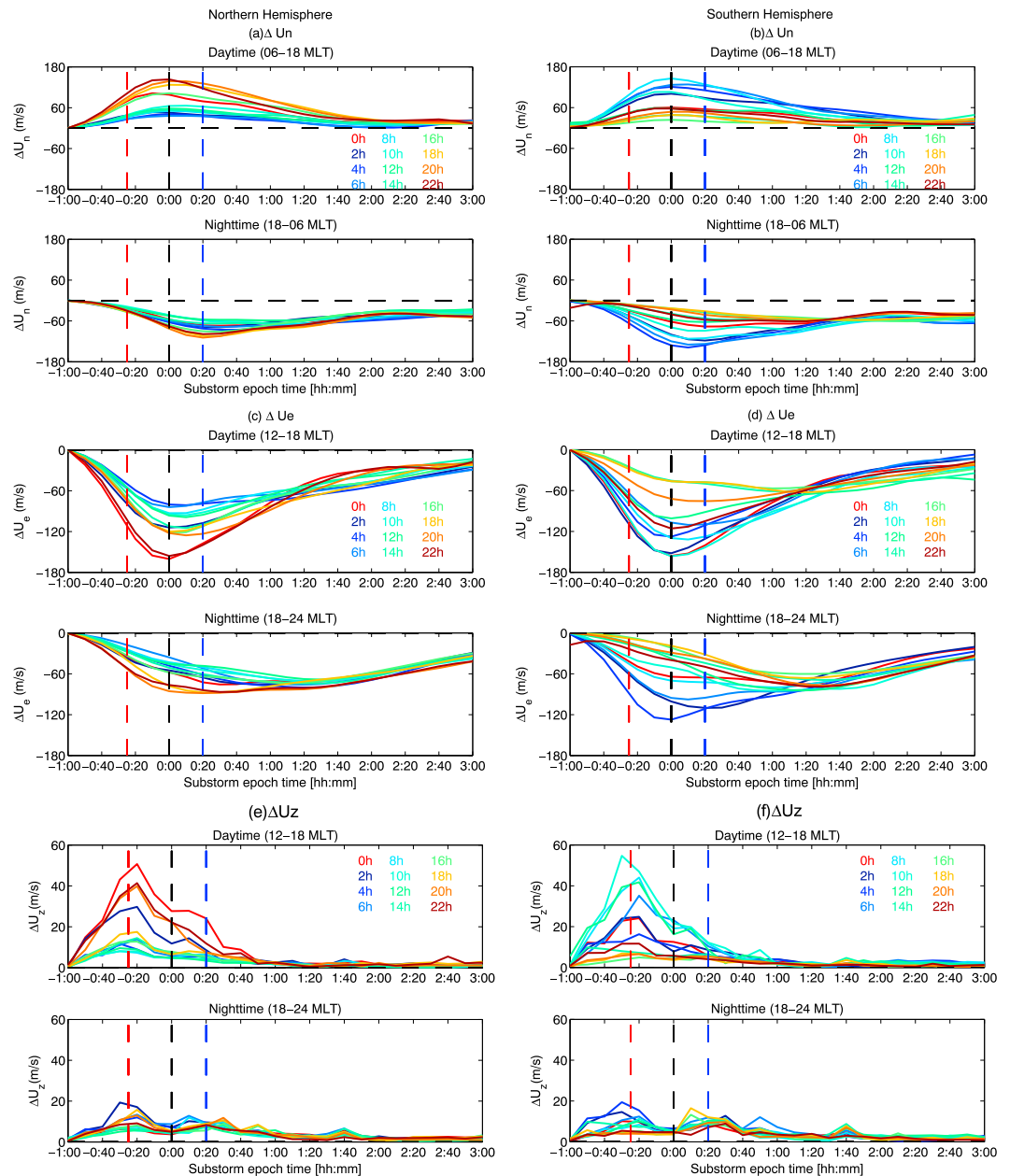


Figure 8. Substorm time variation of peak disturbed wind in the daytime (0600–1800 MLT) and nighttime (1800–0600 MLT). Different colors represent substorm onset times at 2 h intervals from 0000 to 2200 UT. The onset occurs at 0:00 epoch time, as indicated by the black vertical dashed line. The red (blue) vertical line indicates the time when IMF B_z (HP) reaches a minimum (maximum) value. (a and b) Meridional wind, (c and d) zonal wind, and (e and f) vertical wind. Figures 8a, 8c, and 8e represent the Northern Hemisphere, and Figures 8b, 8d, and 8f represent the right the Southern Hemisphere.

upward wind in the Northern (Southern) Hemisphere. In most cases, the variations with UT in the disturbed winds are larger in the daytime in comparison to the nighttime and larger in the Southern Hemisphere than in the Northern Hemisphere.

4.5. Dependence on Solar Zenith Angle

The solar illumination (i.e., SZA) is related to the geographic latitude (GLat). At a given MLAT and MLT sector the corresponding GLat exhibits variation with UT and longitude. For example, 65° MLAT/1500 MLT in the Northern Hemisphere corresponds to 54° GLat/21:00 UT at near-pole longitudes (90°W geographic longitude, GLon) but corresponds to 69° GLat/09:00 UT at far-from-pole longitudes (90°E GLon). Thus, more sunlight

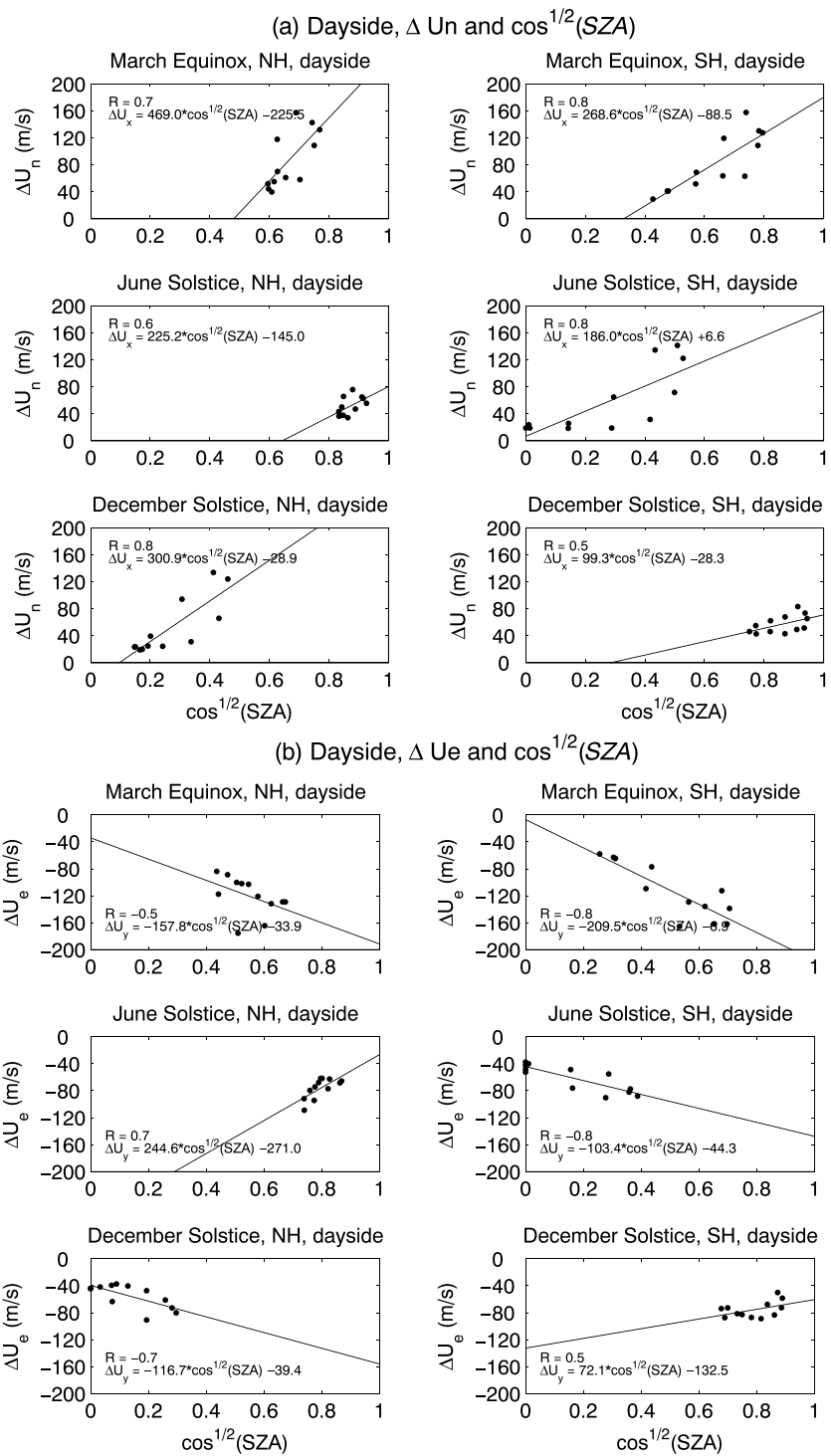


Figure 9. Correlation analysis of peak (a) meridional disturbed wind and (b) zonal disturbed wind with $\cos^{1/2}(\text{SZA})$ (solar zenith angle, SZA) in the daytime. SZA is calculated at 1500 MLT and $\pm 65^\circ$ MLAT. In each subplot, from top to bottom results are illustrated for March equinox, June solstice, and December solstice, respectively.

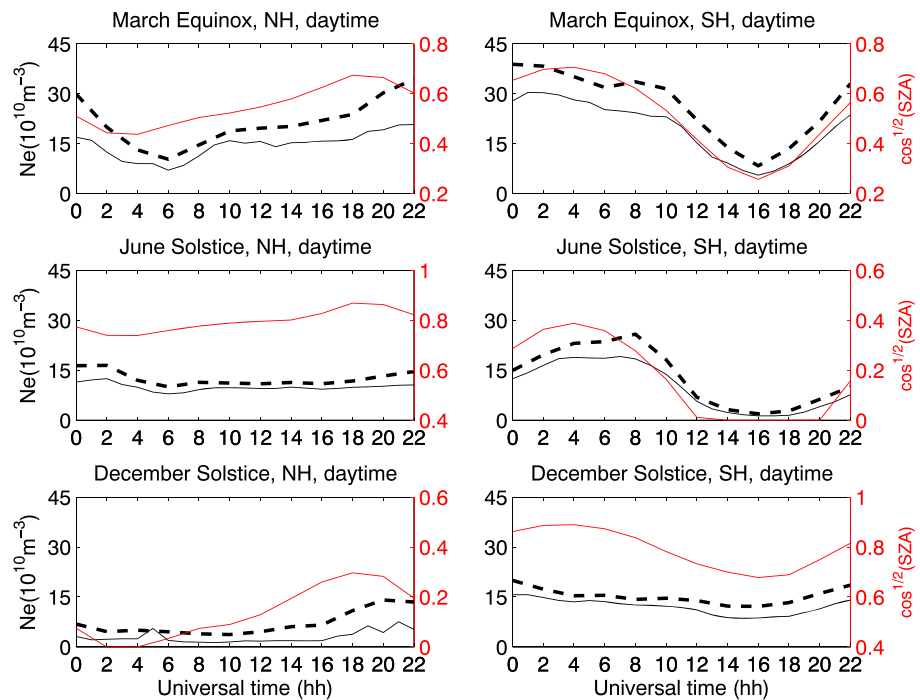


Figure 10. Universal time variations of peak electron density for the quiet time runs are shown as black full line in the daytime. Peak electron densities during substorm periods starting at different UT times are shown as black dashed lines. $\cos^{1/2}(SZA)$ are shown as red curves. SZA is calculated at 1500 MLT and $\pm 65^\circ$ MLAT.

is received at 21:00 UT at near-pole longitudes ($90^\circ W$ GLon) in comparison to 09:00 UT at far-from-pole longitudes ($90^\circ E$ GLon).

The peak values of meridional and zonal disturbed winds were identified from Figure 8 for all substorm events, which correspond to different UT start times. According to Chapman's theory, Ne is proportional to $\cos^{1/2}(SZA)$, where SZA is solar zenith angle. Figure 9 shows the correlation between peak disturbed winds in both poleward and westward direction and $\cos^{1/2}(SZA)$ in the daytime. SZA was calculated at $\pm 65^\circ$ MLAT and 1500 MLT in the Northern and Southern Hemispheres, respectively. The quantitative relationship between the peak disturbed winds and $\cos^{1/2}(SZA)$ for all substorms is shown.

On the dayside disturbed winds correlate well with $\cos^{1/2}(SZA)$ at equinox and in local winter with correlation coefficients > 0.5 . With more solar illumination (smaller SZA and larger $\cos^{1/2}(SZA)$), stronger disturbed winds tend to be generated. This is as expected, because the ion drag is the dominant force acting on the meridional and zonal winds in the daytime. The ion drag force is proportional to the ion density, which is higher in the case of a smaller SZA, i.e., under conditions of more sunlight.

The variation with UT in $\cos^{1/2}(SZA)$ together with peak Ne for both quiet periods and substorm periods are shown together in Figure 10. $\cos^{1/2}(SZA)$ exhibits a wave-1 structure along UT in both hemispheres, with the Northern Hemisphere out of phase with respect to the Southern Hemisphere. The variation with UT in $\cos^{1/2}(SZA)$ is due to the displacement between the geomagnetic and geographic coordinate systems. The variation with UT in solar illumination in the daytime gives rise to the temporal variations in Ne . As shown in Figure 10, Ne during quiet and substorm periods follows the temporal variation in $\cos^{1/2}(SZA)$ quite well at equinox and in local winter.

However, one can notice that in local summer (i.e., June solstice in the Northern Hemisphere and December solstice in the Southern Hemisphere) the temporal variation in the dayside Ne is less pronounced in comparison to that in winter and at equinox. This is because $\cos^{1/2} SZA$ varies slowly when $SZA < 60^\circ$ (in local summer) but quite steeply near the terminator (at equinox and in local winter). This can explain the less obvious variation with UT in Ne in local summer and large variation with UT in winter and equinox. In accordance with this the correlation between disturbed winds and $\cos^{1/2}(SZA)$ in local summer is not strong on the dayside,

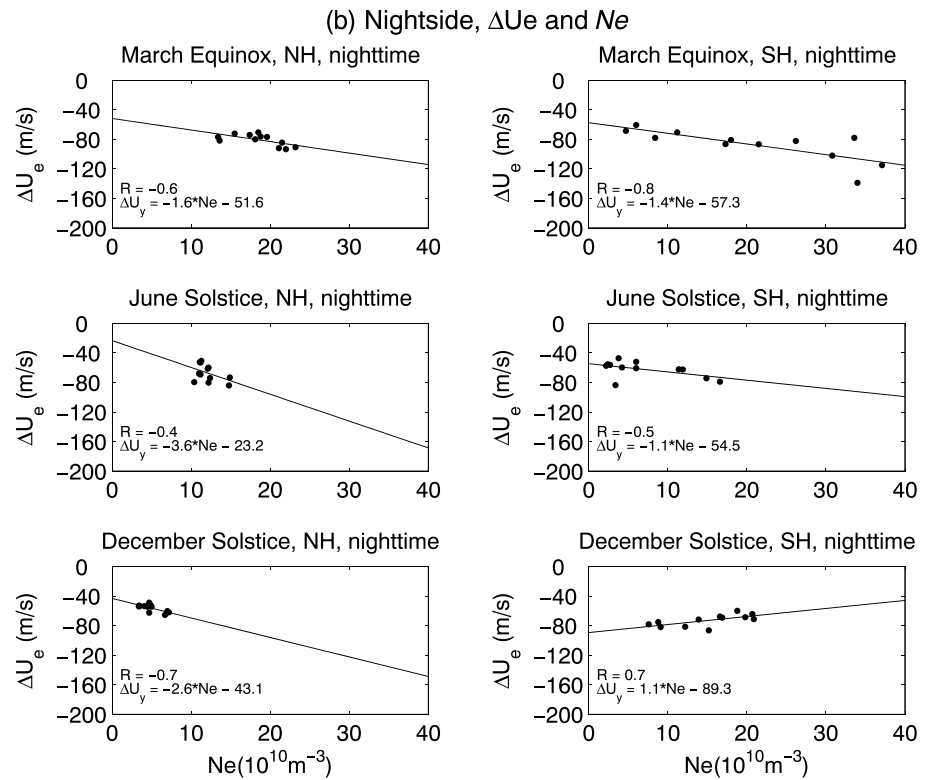
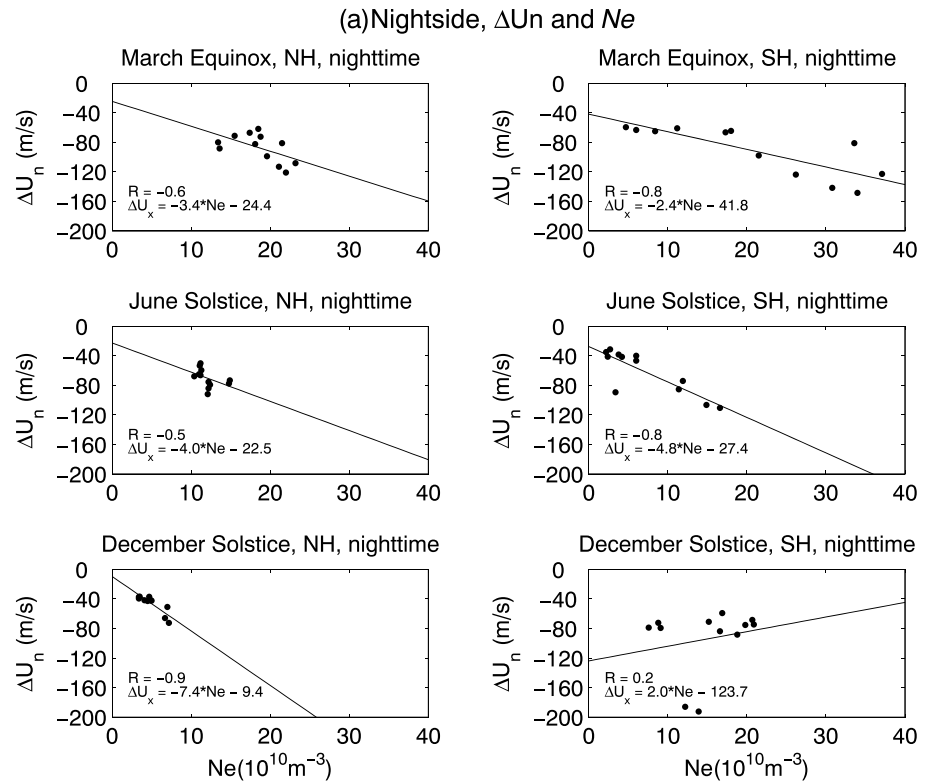


Figure 11. Correlation analysis of peak (a) meridional disturbed wind and (b) zonal disturbed wind with peak electron density on the nightside.

as shown in Figure 9. The result is consistent with previous work at midlatitudes within the ranges of 40°–60° MLAT that the minimum longitudinal differences in N_e occur in summer in comparison to other seasons on the basis of CHAMP observations (see Figure 1) [Wang *et al.*, 2015].

On the basis of the discussion in section 4.2, the disturbed winds on the nightside display a more complicated response to substorms starting at different UT, as several physical processes act together. However, the effects of ion drag are still clear at equinox and in local winter. As shown in Figure 11, there is a strong correlation between peak N_e and peak meridional and zonal disturbed winds on the nightside at equinox and in local winter exhibiting correlation coefficients mostly larger than 0.5. This indicates the dominant role of ion drag during these seasons. Exceptions occur in local summer for both wind components in the Southern Hemisphere and for the zonal wind in the Northern Hemisphere. This might be explained by the fact that the ion drag force is smoothed out by the principal heating of the auroral belt occurring at this season.

All the above cases were rerun with the use of a centered dipole field model with the geographic and geomagnetic poles coinciding with each other. It turns out that the variations with UT in the disturbed winds disappear in the three directions (figures not shown). This is because there is no longitudinal asymmetry in solar illumination and electron density when the geomagnetic and geographic coordinates overlap [Wang *et al.*, 2015]. Therefore, the ion drag forces make little UT/longitudinal differences in the disturbed neutral winds during substorm periods.

5. Summary

The present work investigates the temporal and spatial variations in thermospheric winds at an altitude of 400 km in response to substorms that commence at different universal times (UT) by using GITM simulations. During the substorm period the neutral winds at high latitudes are greatly strengthened, mainly in the poleward, westward, and upward directions at dusk and in the equatorward, westward, and upward directions on the nightside. The response displays an obvious variation with local time, with the perturbations due to variations in B_z peaking in the afternoon sector and those due to both B_z and HP input peaking on the nightside. On the dayside, ion drag forces are predominant driving forces for meridional and zonal disturbance winds, whereas Joule heating is dominant for the vertical disturbed wind. On the nightside the mechanisms for meridional and zonal disturbed winds are a combination of ion drag, Joule heating, and heating of the auroral belt, whereas for the vertical disturbed wind, the heating of the auroral belt is dominant. Viscous force acts as effective resistance to ion drag, while the Coriolis force effect is weak. The peak disturbed winds at equinox and in local winter exhibit large variations with UT in amplitude for different substorms commencing at different UT. With more solar illumination, stronger disturbed winds can be generated. The variation with UT of solar EUV ionization arises from the displacement of the geomagnetic and geographic coordinate systems. The solar illumination effect is less prominent in local summer. In the daytime this is related to the weak UT variation of ion density in full sunlight throughout the day. In the nighttime this is related to the fact that the effect of ion drag might be smaller than the effect of auroral heating processes.

Acknowledgments

The operational support of the CHAMP mission by the German Aerospace Center (DLR) is gratefully acknowledged. The CHAMP thermospheric zonal wind data are available at the web site <http://thermosphere.tudelft.nl/accelldrag/data.php>. CHAMP electron data are retrieved through <http://isdc.gfz-potsdam.de> (or contact Jan Rauberg, jan.rauberg@gfz-potsdam.de). We acknowledge the use of GITM developed by University of Michigan (Aaron Ridley, ridley@umich.edu). Simulation data are available from the authors upon request. This work is supported by the National Nature Science Foundation of China (41674153, 41521063, and 41431073).

References

- Babcock, R. R. Jr., and J. V. Evans (1979), Effects of geomagnetic disturbances on neutral winds and temperatures in the thermosphere observed over Millstone Hill, *J. Geophys. Res.*, *84*, 5349–5354, doi:10.1029/JA084iA09p05349.
- Bilitza, D. (2001), International Reference Ionosphere 2000, *Radio Sci.*, *36*, 261–275, doi:10.1029/2000RS002432.
- Blanc, M., and A. D. Richmond (1980), The ionospheric disturbance dynamo, *J. Geophys. Res.*, *85*, 1669–1686, doi:10.1029/JA085iA04p01669.
- Clausen, L. B. N., S. E. Milan, and A. Grocott (2014), Thermospheric density perturbations in response to substorms, *J. Geophys. Res. Space Physics*, *119*, 4441–4455, doi:10.1002/2014JA019837.
- Deng, W., T. L. Killeen, A. G. Burns, R. G. Roble, J. A. Slavin, and L. E. Wharton (1993), The effects of neutral inertia on ionospheric currents in the high-latitude thermosphere following a geomagnetic storm, *J. Geophys. Res.*, *98*, 7775–7790, doi:10.1029/92JA02268.
- Deng, Y., and A. J. Ridley (2006), Dependence of neutral winds on convection E -field, solar EUV, and auroral particle precipitation at high latitudes, *J. Geophys. Res.*, *111*, A09306, doi:10.1029/2005JA011368.
- Deng, Y., and A. J. Ridley (2007), Possible reasons for underestimating Joule heating in global models: E field variability, spatial resolution, and vertical velocity, *J. Geophys. Res.*, *112*, A09308, doi:10.1029/2006JA012006.
- Deng, Y., T. J. Fuller-Rowell, R. A. Akmaev, and A. J. Ridley (2011), Impact of the altitudinal Joule heating distribution on the thermosphere, *J. Geophys. Res.*, *116*, A05313, doi:10.1029/2010JA016019.
- Emmert, J. T., B. G. Fejer, C. G. Fesen, G. G. Shepherd, and B. H. Solheim (2001), Climatology of middle- and low-latitude daytime F region disturbance neutral winds measured by Wind Imaging Interferometer (WINDII), *J. Geophys. Res.*, *106*, 24,701–24,712, doi:10.1029/2000JA000372.
- Emmert, J. T., B. G. Fejer, G. G. Shepherd, and B. H. Solheim (2002), Altitude dependence of middle and low-latitude daytime thermospheric disturbance winds measured by WINDII, *J. Geophys. Res.*, *107*, 1483, doi:10.1029/2002JA009646.

- Emmert, J. T., M. L. Faivre, G. Hernandez, M. J. Jarvis, J. W. Meriwether, R. J. Niciejewski, D. P. Sipler, and C. A. Tepley (2006a), Climatologies of nighttime upper thermospheric winds measured by ground-based Fabry-Perot interferometers during geomagnetically quiet conditions: 1. Local time, latitudinal, seasonal, and solar cycle dependence, *J. Geophys. Res.*, *111*, A12302, doi:10.1029/2006JA011948.
- Emmert, J. T., G. Hernandez, M. J. Jarvis, R. J. Niciejewski, D. P. Sipler, and S. Vennerstrom (2006b), Climatologies of nighttime upper thermospheric winds measured by ground-based Fabry-Perot interferometers during geomagnetically quiet conditions: 2. High-latitude circulation and interplanetary magnetic field dependence, *J. Geophys. Res.*, *111*, A12303, doi:10.1029/2006JA011949.
- Emmert, J. T., A. D. Richmond, and D. P. Drob (2010), A computationally compact representation of magnetic-apex and quasi-dipole coordinates with smooth base vectors, *J. Geophys. Res.*, *115*, A08322, doi:10.1029/2010JA015326.
- Ercha, A., A. J. Ridley, D. Zhang, and Z. Xiao (2012), Analyzing the hemispheric asymmetry in the thermospheric density response to geomagnetic storms, *J. Geophys. Res.*, *117*, A08317, doi:10.1029/2011JA017259.
- Frey, H. U., and S. B. Mende (2006), Substorm onsets as observed by IMAGE-FUV, *Int. Conf. Substorms*, *8*, 71–75.
- Fujiwara, H., S. Maeda, H. Fukunishi, T. Fuller-Rowell, and D. Evans (1996), Global variations of thermospheric winds and temperatures caused by substorm energy injection, *J. Geophys. Res.*, *101*(A1), 225–239.
- Fuller-Rowell, T. J., and D. S. Evans (1987), Height-integrated Pedersen and Hall conductivity patterns inferred from the TIROS-NOAA satellite data, *J. Geophys. Res.*, *92*, 7606–7618, doi:10.1029/JA092iA07p07606.
- Fuller-Rowell, T. J., M. V. Codrescu, R. J. Moffett, and S. Quegan (1994), Response of the thermosphere and ionosphere to geomagnetic storms, *J. Geophys. Res.*, *99*, 3893–3914, doi:10.1029/93JA02015.
- Hagan, M. E., M. D. Burrage, J. M. Forbes, J. Hackney, W. J. Randel, and X. Zhang (1999), GSWM-98: Results for migrating solar tides, *J. Geophys. Res.*, *104*, 6813–6828, doi:10.1029/1998JA900125.
- Hedin, A. E. (1991), Extension of the MSIS thermosphere model into the middle and lower atmosphere, *J. Geophys. Res.*, *96*, 1159–1172, doi:10.1029/90JA02125.
- Killeen, T. L., and R. Roble (1984), An analysis of the high-latitude thermospheric wind pattern calculated by a thermospheric general circulation model: 1 Momentum forcing, *J. Geophys. Res.*, *89*, 7509–7522, doi:10.1038/381766a0.
- Liu, X., and A. Ridley (2015), A simulation study of the thermosphere mass density response to substorms using GITM, *J. Geophys. Res. Space Physics*, *120*, 7987–8001, doi:10.1002/2014JA020962.
- Lühr, H., S. Rentz, P. Ritter, H. Liu, and K. Häusler (2007), Average thermospheric wind patterns over the polar regions, as observed by CHAMP, *Ann. Geophys.*, *25*, 1093–1101.
- Lyatsky, W., P. T. Newell, and A. Hamza (2001), Solar illumination as cause of the equinoctial preference for geomagnetic activity, *Geophys. Res. Lett.*, *28*(12), 2353–2356, doi:10.1029/2000GL012803.
- Lyons, L. R. (1996), Substorms: Fundamental observational features, distinction from other disturbances, and external triggering, *J. Geophys. Res.*, *101*, 13,011–13,026.
- Maus, S., et al. (2005), The 10th generation international geomagnetic reference field, *Phys. Earth Planet. Inter.*, *151*, 320–322, doi:10.1016/j.pepi.2005.03.006.
- McCormac, F. G., and R. W. Smith (1984), The influence of the interplanetary magnetic field *Y* component on the ion and neutral motions in the polar thermosphere, *Geophys. Res. Lett.*, *11*, 935–938.
- Pawłowski, D. J., and A. J. Ridley (2009), Modeling the ionospheric response to the 28 October 2003 solar flare due to coupling with the thermosphere, *Radio Sci.*, *44*, RS0A23, doi:10.1029/2008RS004081.
- Perlongo, N. J., and A. J. Ridley (2016), Universal time effects in the response of the thermosphere to electric field changes, *J. Geophys. Res. Space Physics*, *121*, 3681–3698, doi:10.1002/2015JA021636.
- Richmond, A. D. (1995), Ionospheric electrodynamics using magnetic apex coordinates, *J. Geophys. Res.*, *47*, 191–212.
- Richmond, A. D., and S. Matsushita (1975), Thermospheric response to a magnetic substorm, *J. Geophys. Res.*, *80*, 2839–2850, doi:10.1029/JA080i019p02839.
- Richmond, A. D., C. Lathuillere, and S. Vennerstroem (2003), Wind in the high-latitude lower thermosphere: Dependence on the interplanetary magnetic field, *J. Geophys. Res.*, *108*, doi:10.1029/2002JA009493.
- Ridley, A. J., Y. Deng, and G. Tóth (2006), The global ionosphere thermosphere model, *J. Atmos. Terr. Phys.*, *68*, 839–864, doi:10.1016/j.jastp.2006.01.008.
- Rishbeth, H. (1967), The effect of winds on the ionospheric F_2 -peak, *J. Atmos. Terr. Phys.*, *29*, 225–238, doi:10.1016/0021-9169(67)90192-4.
- Ritter, P., H. Lühr, and E. Doornbos (2010), Substorm-related thermospheric density and wind disturbances derived from CHAMP observations, *Ann. Geophys.*, *28*, 1207–1220.
- Robinson, R. M., R. R. Vondrak, K. Miller, T. Dabbs, and D. A. Hardy (1987), On calculating ionospheric conductances from the flux and energy of precipitating electrons, *J. Geophys. Res.*, *92*(A3), 2565–2569.
- Roble, R. G., R. E. Dickinson, and E. C. Ridley (1982), Global circulation and temperature structure of thermosphere with high-latitude plasma convection, *J. Geophys. Res.*, *87*, 1599–1614, doi:10.1029/JA087iA03p01599.
- Russell, C. T., and R. L. McPherron (1973), Semiannual variation of geomagnetic activity, *J. Geophys. Res.*, *78*, 92–108, doi:10.1029/JA078i001p00092.
- Temerin, M., and X. Li (2002), A new model for the prediction of *Dst* on the basis of the solar wind, *J. Geophys. Res.*, *107*, 1472, doi:10.1029/2001JA007532.
- Thayer, J. P., and T. L. Killeen (1993), A kinematic analysis of the high-latitude thermospheric neutral circulation pattern, *J. Geophys. Res.*, *98*, 11,549–11,565, doi:10.1029/93JA00629.
- Thayer, J. P., T. L. Killeen, F. G. McCormac, C. R. Tschan, J. Ponthieu, and N. W. Spencer (1987), Thermospheric neutral wind signatures dependent on the east-west component of the interplanetary magnetic field for Northern and Southern Hemispheres as measured from Dynamics Explorer-2, *Ann. Geophys.*, *5*, 363–368.
- Wang, H., and H. Lühr (2007), Seasonal-longitudinal variation of substorm occurrence frequency: Evidence for ionospheric control, *Geophys. Res. Lett.*, *34*, L07104, doi:10.1029/2007GL029423.
- Wang, H., and H. Lühr (2016), Longitudinal variation in zonal winds at subauroral regions: Possible mechanisms, *J. Geophys. Res. Space Physics*, *121*, 745–763, doi:10.1002/2015JA022086.
- Wang, H., H. Lühr, and S. Y. Ma (2012), The relation between subauroral polarization streams, westward ion fluxes, and zonal wind: Seasonal and hemispheric variations, *J. Geophys. Res.*, *117*, A04323, doi:10.1029/2011JA017378.
- Wang, H., A. Ridley, and J. Zhu (2015), Theoretical study of zonal differences of electron density at midlatitudes with GITM simulation, *J. Geophys. Res. Space Physics*, *120*, 2951–2966, doi:10.1002/2014JA020790.
- Weimer, D. R. (1996), A flexible, IMF dependent model of high-latitude electric potentials having “space weather” applications, *Geophys. Res. Lett.*, *23*, 2549–2552, doi:10.1029/96GL02255.

- Weimer, D. R. (2005), Improved ionospheric electrodynamic models and application to calculating Joule heating rates, *J. Geophys. Res.*, *110*, A05306, doi:10.1029/2004JA010884.
- Xiong, C., H. Lühr, and B. G. Fejer (2015a), Global features of the disturbance winds during storm time deduced from CHAMP observations, *J. Geophys. Res.*, *120*, 5137–5150, doi:10.1002/2015JA021302.
- Xiong, C., Y.-L. Zhou, H. Lühr, and S.-Y. Ma (2015b), Tidal signatures of the thermospheric mass density and zonal wind at midlatitude: CHAMP and GRACE observations, *Ann. Geophys.*, *33*, 185–196, doi:10.5194/angeo-33-185-2015.
- Yigit, E., and A. J. Ridley (2011), Effects of high-latitude thermosphere heating at various scale sizes simulated by a nonhydrostatic global thermosphere-ionosphere model, *J. Atmos. Terr. Phys.*, *73*, 592–600, doi:10.1016/j.jastp.2010.12.003.
- Zhu, J., and A. J. Ridley (2014), The effect of background conditions on the ionospheric response to solar flares, *J. Geophys. Res. Space Physics*, *119*, 5060–5075, doi:10.1002/2014JA019887.
- Zhu, J., A. J. Ridley, and Y. Deng (2016), Simulating electron and ion temperature in a global ionosphere thermosphere model: Validation and modeling an idealized substorm, *J. Atmos. Sol. Terr. Phys.*, *138*, 243–260, doi:10.1016/j.jastp.2016.01.005.